

PEnG: Pose-Enhanced Geo-Localisation

Tavis Shore¹ and Oscar Mendez¹ and Simon Hadfield¹

Abstract—Cross-view Geo-localisation is typically performed at a coarse granularity, because densely sampled satellite image patches overlap heavily. This heavy overlap would make disambiguating patches very challenging. However, by opting for sparsely sampled patches, prior work has placed an artificial upper bound on the localisation accuracy that is possible. Even a perfect oracle system cannot achieve accuracy greater than the average separation of the tiles. To solve this limitation, we propose combining cross-view geo-localisation and relative pose estimation to increase precision to a level practical for real-world application. We develop PEnG, a 2-stage system which first predicts the most likely edges from a city-scale graph representation upon which a query image lies. It then performs relative pose estimation within these edges to determine a precise position. PEnG presents the first technique to utilise both viewpoints available within cross-view geo-localisation datasets to enhance precision to a sub-metre level, with some examples achieving centimetre level accuracy. Our proposed ensemble achieves state-of-the-art precision - with relative Top-5m retrieval improvements on previous works of 213%. Decreasing the median euclidean distance error by 96.90% from the previous best of 734m down to 22.77m, when evaluating with 90° horizontal FOV images. Code will be made available: tavisshore.co.uk/PEnG.

Keywords: Localisation, Vision-Based Navigation, Computer Vision for Transportation

I. INTRODUCTION

Localisation is vital in the majority of mobile robotics applications. Common techniques such as Global Navigation Satellite Systems (GNSS) provide absolute positioning data to clients. These are prone to failure in certain environments. One example are dense urban canyons such as New York City where tall buildings cause signal occlusions & reflections, preventing successful satellite communication. Another example are regions of conflict where malicious actors purposefully disrupt positioning by spoofing signals, inserting erroneous information.

Image localisation may provide a solution as agents can fully self-localise using onboard sensors, removing requirements for external communication. These techniques aim to relate an agent’s query image with previously seen geo-tagged images, determining an updated position according to feature and positional similarities with these references. A large proportion of mobile robots are already equipped with cameras, increasing the viability of image localisation.

Cross-View Geo-localisation (CVGL) is an increasingly popular branch of image localisation research, offering a

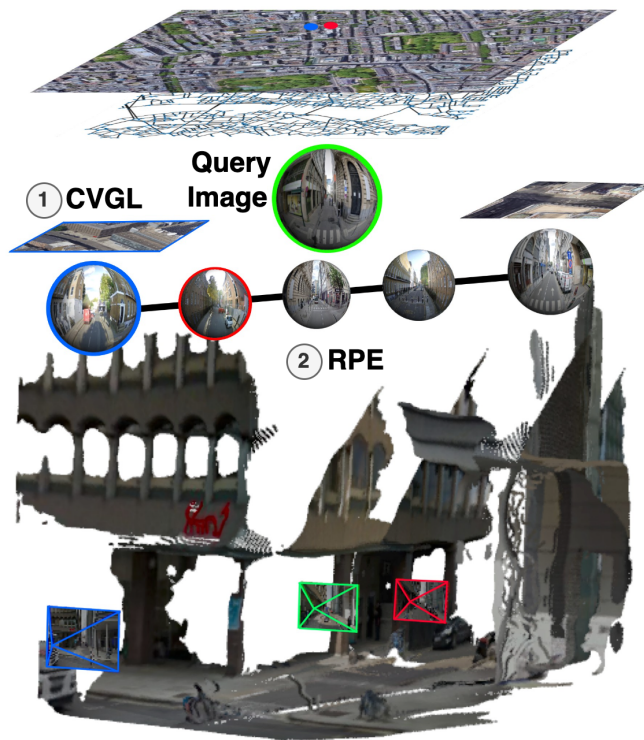


Fig. 1: PEnG Stages: 1) City-scale satellite image with underlying graph network, CVGL estimates candidate edges within city’s graph. 2) Pose estimation along these edges achieves refined geographic poses. Green denotes a query input, blue and red display two known reference images.

viable form of generalisable wide-scale image localisation. The objective is to relate a street-level query image to a database of reference satellite images - returning the geographic coordinates of the highest correlating known satellite image.

Pose estimation is a related field aiming to determine a camera’s pose within a scene. These techniques generally operate at a smaller scale than CVGL, localising within a few metres, instead of whole cities. They generally operate as continuous prediction, rather than retrieval problems, and operate in N-Degrees of Freedom (DoF) as opposed to simple geographic coordinates. Pose estimation has two primary sub-fields - Absolute Pose Estimation (APE) and Relative Pose Estimation (RPE). APE aims to determine a camera’s position and orientation within a 3D world coordinate frame. RPE aims to compute the same, but with respect to a reference camera.

¹ Centre for Vision Speech and Signal Processing, University of Surrey, Guildford, United Kingdom, {t.shore, o.mendez, s.hadfield}@surrey.ac.uk

We propose leveraging the advantages of both techniques in a single two-stage system to achieve high-precision city-scale localisation, shown in top-down order in Figure 1. Taking as input a street-level image - the first stage performs city-wide CVGL, predicting the most recently observed road junction. Operating the CVGL stage at the scale of road junctions, helps to keep the reference set lean and discriminative, ensuring efficient and accurate retrieval results of coarse location. The second stage takes the CVGL sub-region predictions and performs RPE along neighbouring roads, merging likelihoods from both stages to determine a final 3-DoF pose. This novel combination of learned computer vision techniques achieves a reduction in the median localisation error from 734m to 22.77m, evaluating with 90° crops of the StreetLearn dataset [1].

In summary, our research contributions are:

- Introduce the first technique for performing precise image localisation in a city-scale by utilising information from both image viewpoints in CVGL datasets.
- Introduce emulating a simple compass, filtering reference embeddings according to a configurable yaw threshold, greatly increasing localisation precision.
- Demonstrate strong generalisation to cities not seen in training - localising with a median error of 22.77m within the large dense region of Manhattan, considering a region area of $36.1km^2$.

II. RELATED WORKS

A. Camera Pose Estimation

RPE can be divided into two categories: feature matching, and pose regression. More traditional camera localisation techniques often utilise structure-based methods, representing a scene with an explicit SfM or SLAM reconstruction [2], [3], [4]. This often requires a large number of images to have already been captured within a scene, limiting generalisation.

Shotton et al. [5] introduce a novel method called Scene Coordinate Regression Forest (SCoRe Forest) for inferring the pose of an RGB-D camera relative to a known 3D scene using a single image with decision forests. Kendall et al. propose PoseNet [6], the first CNN designed for end-to-end 6-DOF camera pose localisation, evaluating the network thoroughly to prove the viability of deep learning for the field. In their following paper [7], they apply a principled loss function based on the scene’s geometry to learn camera pose without any hyper-parameters, achieving state of the art (SOTA) results, reducing the performance gap to traditional methods. Sattler et al. [4] propose using a prioritised matching approach, considering features more likely to yield 2D-to-3D matches, terminating searches once sufficient matches have been found. Brachmann et al. [8] propose *DSAC*, a differentiable counterpart to RANSAC, replacing the deterministic hypothesis selection with a probabilistic selection, deriving the expected loss with respect to all learnable parameters. Applying this to image localisation achieved higher accuracies than previous deep learning based methods. Clark et al. [9] propose extending to sequential

camera pose estimation, designing an RNN which achieves smoothed poses and greatly reduced localisation error. Sarlin et al [10] propose *HFNet* - performing coarse-to-fine image localisation by predicting local features and global descriptors for 6-DoF localisation simultaneously. Map-free Relocalisation [11] introduces using a single photo from a scene for metric scaled re-localisation, negating the requirement to construct a scaled map of the scene. Rockwell et al. [12] propose *FAR*, combining correspondence estimation and pose regression techniques to utilise the benefits from both to provide precision and generalisation. Wang et al. [13] and Leroy et al. in the follow-up paper [14] propose *Dust3r* and *Mast3r* respectively. Both are techniques for dense unconstrained stereo 3D reconstruction of arbitrary image collections, with no prior information. *Mast3r* achieves SOTA performance in various fields including camera calibration and dense 3D reconstruction. Moreau et al. [15] propose *CROSSFIRE* - using NeRFs as implicit scene maps and propose a camera re-localisation algorithm for this representation. *CROSSFIRE* achieves SOTA accuracy and is capable of operating in dynamic outdoor environments.

Similar to how *FAR* proposed combining multiple pose estimation paradigms to achieve SOTA performance in that particular sub-field, we propose combining multiple image localisation techniques to achieve high precision localisation in large scale regions with different input modalities.

B. Cross-View Geo-Localisation

Current CVGL techniques primarily focus on embedding retrieval - extracting reduced dimensionality representations of reference satellite images, aiming to return geo-coordinates from those most similar to query images. Techniques are being increasingly proposed to improve performance by manipulating extracted features, [16], [17], [18].

Workman and Jacobs [19] first propose CNNs for learning feature relationships across viewpoints. This was extended by Lin et al. [20], treating each query uniquely, utilising euclidean similarities for retrieval. Vo and Hays [21] add rotation information through an auxiliary loss, evaluating misalignment impact. CVM-Net [22] add NetVLAD [23] to the CNN, aggregating local feature residuals to cluster centroids. Liu and Li [24] increase access to orientation information, improving the latent space robustness. Shi et al. [25] developed a spatial attention mechanism, improving feature alignment between views. In [26] they increase the cross-view feature similarity, by applying the techniques to limited-Field-of-View (FOV) data. This was important due to the ubiquity of monocular cameras compared with panoramic cameras, increasing feasibility. [27] computes feature correlation between ground-level images and polar-transformed aerial images, shifting and cropping at the strongest alignment before performing image retrieval. Toker et al. [28] synthesised streetview images from aerial image queries before performing image retrieval. L2LTR [29] developed a CNN+Transformer network, combining a ResNet backbone with a vanilla ViT encoder to increase performance over

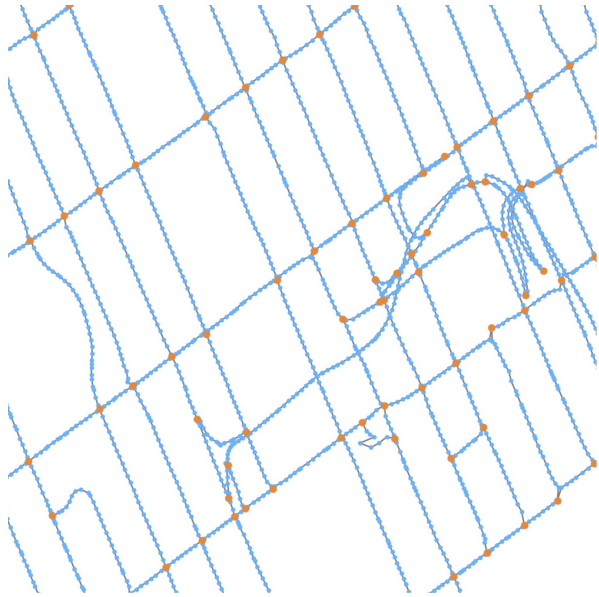


Fig. 2: Section of Manhattan graph with primary (orange) and secondary (blue) nodes displayed. Most edges have a constant yaw, motivating the utilisation of a compass.

SOTA. TransGeo [16] proposed a transformer that uses an attention-guided non-uniform cropping strategy to remove uninformative areas.

In GeoDTR [30], [31], Zhang et al. separate geometric information from the raw features, learning spatial correlations within visual features to enhance performance. Zhu et al. introduced SAIG [17], an attention-based CVGL backbone, representing long-range interactions among patches and cross-view associations with multi-head self-attention layers. BEV-CV [18] introduces Birds-Eye-View (BEV) transforms to the field, reducing representational differences between viewpoints to create more similar embeddings. Sample4Geo [32] propose two CVGL sampling strategies, geographically sampling for optimal training initialisation, mining hard-negatives according to feature similarities between viewpoints. SpaGBOL [33] propose progressing the CVGL field from single and sequential representations to graph-based representation, allowing for more geo-spatially strong embeddings.

To date all of the above CVGL approaches have followed a retrieval paradigm where the accuracy of results is limited by the granularity of the geo-referenced database. Sparsely sampled data can lead to higher retrieval rates due to greater feature dissimilarities, while densely sampled data may enhance localisation precision but decrease performance, as overlapping satellite image patches increase the likelihood of incorrect retrievals

III. METHODOLOGY

A. City-Scale Geo-Localisation Data Representation

We frame CVGL as a graph comparison problem, similar to the technique demonstrated in *SpaGBOL* [33]. Where

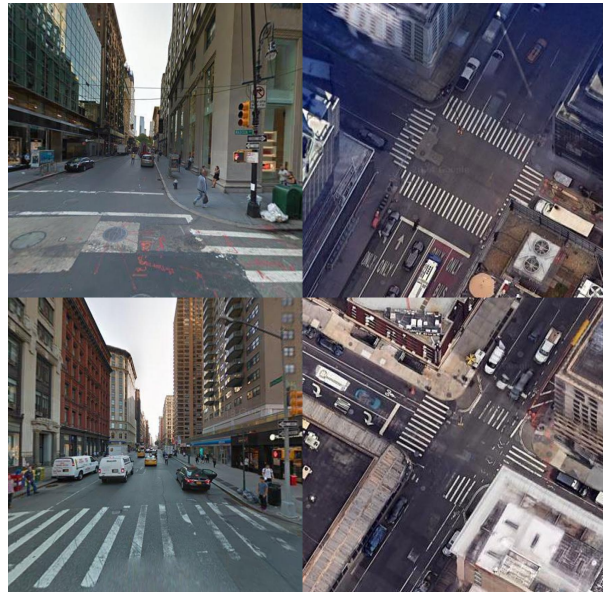


Fig. 3: Example primary node (road junction) cross-view image pairs. Left-hand side shows 90° crops from panoramas and the right-hand side shows aerial images at zoom 20.

SpaGBOL established a lower bound on localisation precision by only applying graph nodes at road junctions, we incorporate orders of magnitude more nodes by placing *secondary nodes* along existing edges, enhancing the density of data. These graphs now have two classes of nodes, denoted *primary nodes* N - representing road junctions, and *secondary nodes* Q - captured along roads at varying intervals. This significant increase in data density greatly increases the precision upper bound. Figure 2 shows a section of this graph representation of Manhattan.

We represent each region in the dataset $i \in \{\text{Manhattan}, \dots\}$ as a separate graph $G_i = (N, Q, E)$ with primary nodes $N_i = \{n_1, n_2, \dots, n_N\}$, secondary nodes $Q_i = \{q_1, q_2, \dots, q_Q\}$, edges $E_i = \{e_{1,2}, e_{1,3}, \dots, e_E\}$. Edges $e_{a,b}$ represent roads connecting primary nodes a and b . Each node in both classes has attributes - $\{I_{sat}, I_{street}, L, \Psi, B\}$, containing a panoramic streetview image and a satellite image - both RGB: $I_j \in \mathbb{R}^{3 \times W \times H}$, $j \in \{\text{street}, \text{sat}\}$, location $L = \{\phi, \lambda\}$ consists of geographical latitude and longitude coordinates, $\Psi \in \mathbb{R} : \{-180^\circ \leq \Psi \leq 180^\circ\}$ is the north-aligned camera yaw, and $B = \{\beta_1, \dots, \beta_K\}$ are north-aligned bearings to K neighbouring nodes - where $\beta \in \mathbb{R} : \{-180^\circ \leq \beta \leq 180^\circ\}$.

We limit the streetview image's (I_{street}) FOV to increase the technique's feasibility as a large proportion of existing vehicles possess monocular cameras. Cameras are assumed to be fixed to the vehicle in a forward-facing configuration. We experiment with FOVs, $\Theta \in \{70^\circ, 90^\circ, 120^\circ\}$.

B. PEnG Procedure

Our proposed technique, PEnG, operates in two stages, described in Figure 4: initially estimating *candidate primary nodes* with graph-based CVGL (shown on the left-hand

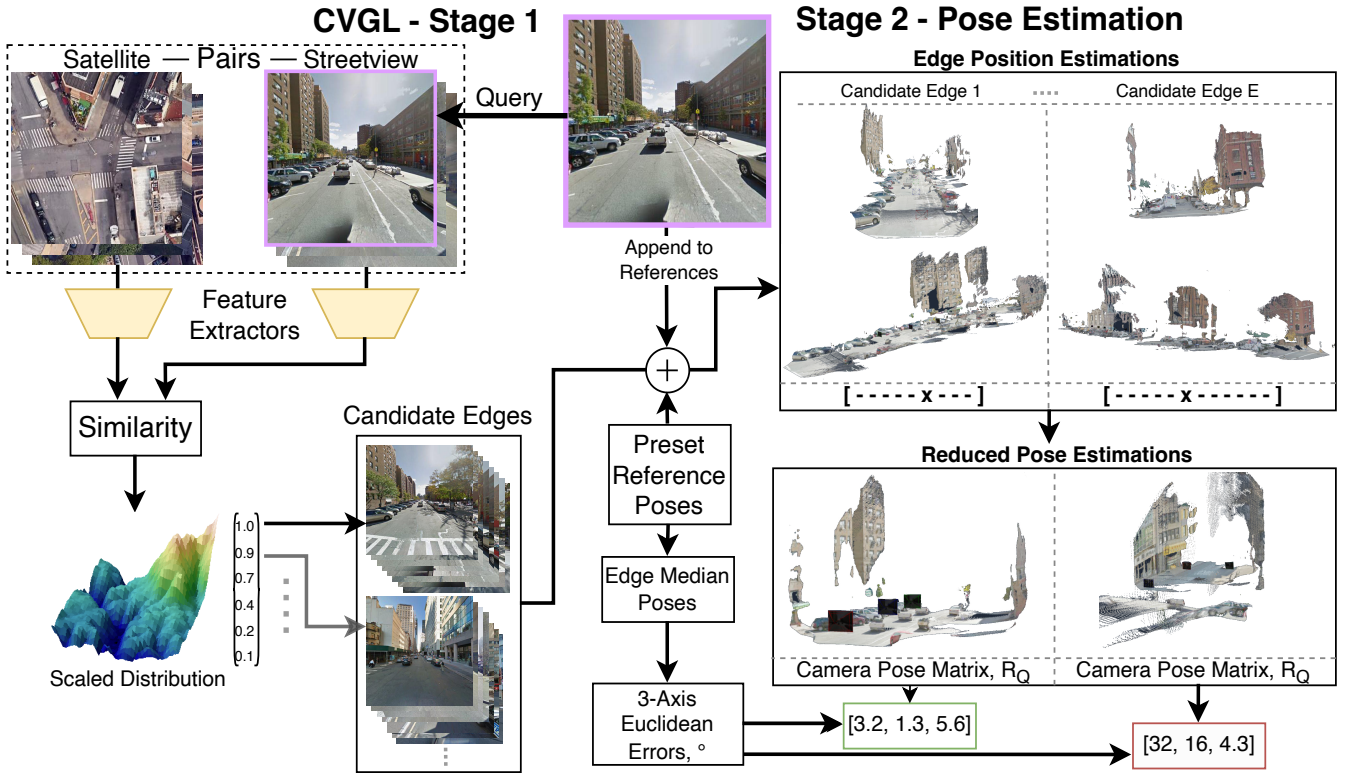


Fig. 4: 2-Stage system diagram. Stage 1 retrieves scaled similarities of reference embeddings for the latest seen primary node, acquiring ordered candidate edges. Stage 2 runs through edges consecutively until a threshold is met or completion. Position along an edge is estimated against all reference images, then estimating pose with the predicted adjacent two images.

side) before performing RPE relative to the secondary nodes present along each *candidate edge* until a threshold is met, or all candidate edges have been processed.

The main purpose of the first stage is to reduce the number of reference images when performing relative pose estimation. This enables city-scale pose estimation as without it, pose estimation takes orders of magnitude longer.

1) *Graph-Based Cross-View Geo-Localisation*: We perform CVGL following the standard procedure as used within previous works [18], [22], [27]. We implement a siamese-like network of CNN feature extractors, with no weight sharing, to produce similar embeddings η_t from corresponding streetview-satellite image pairs. Creating a database of reference embeddings offline, querying this database for retrievals during online operation.

$$\eta_t = \text{CNN}(I_t | \omega_t), t \in \{\text{street}, \text{sat}\} \quad (1)$$

In the first stage, CVGL retrievals are only performed on primary nodes N_i to provide efficient and accurate initial filtering. Retrieved reference embeddings are ordered by descending similarity with the query, and are then min-max normalised to between 0 & 1 giving a confidence score c_i for each candidate node - concluding this stage. Top candidate nodes, C_k , are passed to the second stage depending on the minimum confidence threshold θ_c , and maximum number of

candidates k .

$$c_i = \text{scale} \left(\frac{\eta_i^{\text{query}} \cdot \eta^{\text{ref}}}{\|\eta_i^{\text{query}}\| \|\eta^{\text{ref}}\|}, 0, 1 \right) \quad (2)$$

$$C_k = \{c_i | c_i > \theta_c \text{ and } i < k\} \quad (3)$$

2) *Pose Refinement*: For each candidate node, c , we select that candidate's connected edges, $E_c = \{e_{i,j} | i = c \text{ or } j = c\}$. We then filter these edges by matching the compass heading and the edge's yaw within the graph. For every remaining candidate edge, we then perform RPE in two stages: first estimating a coarse position of the query image along an edge before refining this relative to the two neighbouring reference secondary nodes. The calculation of median edge rotational pose is displayed in Figure 5.

Inspired by [14], we determine the relative pose of query images against each candidate edge's secondary node, before combining the poses across the entire edge. For each image pair along an edge I^1 & I^2 , we determine the set of cross-image pixel correspondences. We then use a transformer-based network to predict 3D pointmaps, $X^{1,1}, X^{1,2}$, from 2D points x^i between these images, expressed in the coordinate frame of I^1 . The pointmaps are then compared $X^{1,1} \leftrightarrow X^{1,2}$, computing the relative poses with RANSAC & PnP [34] expressed in equations 4 and 5.

The objective of PnP is to minimise the reprojection error between the 3D points and their corresponding 2D image

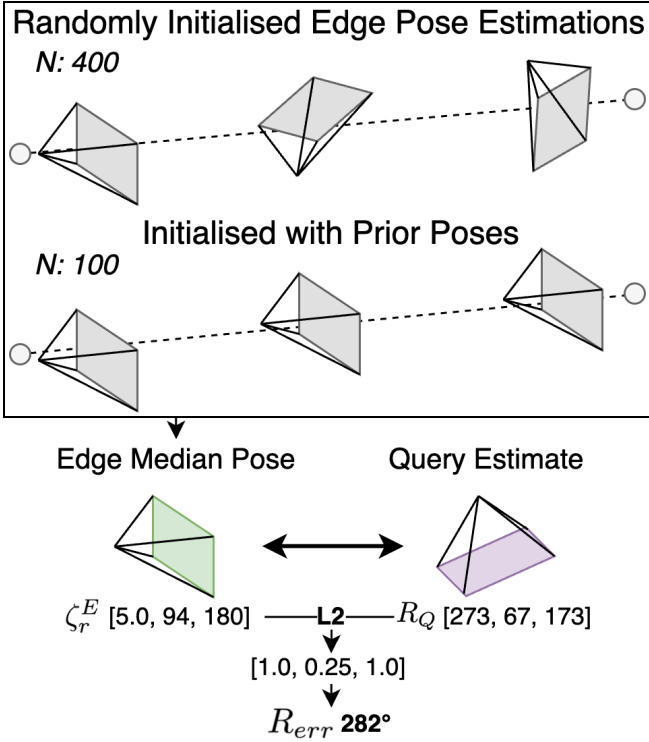


Fig. 5: Pose estimates within each candidate edge are scored by their 3-axis euclidean distance with the mean rotational pose of the secondary nodes. This is possible due to the known orientations of edges within graph representations.

projections:

$$x^i = K(RX^i + t) \quad (4)$$

Where x^i is the projected 2D point, X^i is the 3D world point, K is the estimated camera intrinsic matrix, R & t are the rotation and translation matrices. RANSAC randomly samples 4 points for PnP, optimising the objective to estimate R and t .

We compute the reprojection error as $e_i = \|x_i - K(RX_i + T)\|$, rejecting outliers based on a predefined threshold ϵ . We then maximise the number of inliers $e_i \leq \epsilon$ to achieve the best pose estimate (R^*, t^*) :

$$(R^*, t^*) = \operatorname{argmax}_{R,t} \sum_i \mathbf{1}(e_i \leq \epsilon) \quad (5)$$

where $(e_i \leq \epsilon)$ is the indicator function - equals 1 if e_i is less than or equal to a predefined threshold ϵ , 0 otherwise.

Precomputation - All reference poses, P^r , are estimated prior to system operation, calculating a median 3-DoF rotational matrix for each edge ζ_r^E . As this is a preprocessing step, a larger number of iterations are used compared to during inference. These pre-determined poses then initialise optimisation processes during operation, reducing the required number of iterations - leading to lower operating times without effecting performance.

Operation - Algorithm 1 is executed for each query image, until thresholds such as Maximum Rotational Error

Algorithm 1 PEEnG Algorithm

Require: Graph $G = (N, Q, E)$, Reference Primary Node Database η_N^{sat} , Query and Reference images I_Q^{street} I_R^{sat} , Thresholds $\theta_x \in \{\theta_{pe}, \theta_n, \dots\}$, Reference Poses ζ_r^E

Ensure: R_Q

1: **Stage 1 - CVGL**

2: $\eta^{street} = \text{CNN}(I^{street})$

3: $S = \text{scale}\left(\left(\sum_k \eta_{ik}^{ref} \eta_k^{query}\right), 0, 1\right)$

4:

5: **Stage 2 - Pose Estimation**

6: $i = 0$

7: **while** $\text{thres}(R_{err} \leq \theta_x)$ **do**

$E_{cand} = \text{filter}(N(S_i), \Psi)$

$I^{pairs} = \text{exhaustive}(E_{cand} + I^{street})$

$t_p = \text{RPE}_{position}(I^{pairs})$

$(R^i, t^i) = \text{RPE}_{pose}(I^{t_{p-1}}, I^{t_{p+1}})$

$R_{err}^i = \text{sim}_{euc}(R^i, E_{cand})$

$i = i + 1$

8:

9: **return** Absolute Pose Estimations R_Q

θ_{re} or No. Candidate Nodes θ_n are achieved. Rotational error R_{err} is the 3-DoF summed euclidean distance between the query rotation R_Q and the median edge rotation ζ_r^E . This is calculated with an $[X, Y, Z]$ axis weighting of $[1, 0.25, 1]$ as roll has a smaller impact on performance. Where a query has multiple pose estimations and an L2 distance threshold has not been met, each pose is given a confidence score - rotational errors are summed and min-max scaled to between 0 & 1. Confidence scores from both stages are considered to determine a final pose estimation, calculated by scaling the relative poses to between the edge's ground truth limits.

IV. RESULTS

A. Datasets

The feature extractors for both PEEnG and previous works are trained with the CVUSA dataset [35], cropping streetview images to various FOVs, portraying front-facing road-aligned monocular images. This dataset contains 35,532 streetview-satellite training pairs and 8,884 validation pairs. CVUSA satellite images have a resolution of 750×750 and streetview panoramas of 1232×224 , both north-aligned. We evaluate with the StreetLearn Manhattan dataset [1]. Example image pairs are shown in Figure 3. Manhattan is selected for evaluation as it qualifies as an urban canyon - an environment category that often experiences GNSS failure. The city's data are converted from unconnected images into a graph representation. This contains 53,289 images, comprising 2,622 primary nodes and 50,667 secondary nodes. The graph covers approximately 31.6km^2 . Satellite images are north-aligned with a resolution of 0.20metres/pixel covering 50m^2 (some images may have been captured from drones and other aerial image sources). Streetview images are yaw-aligned panoramas with a resolution of 1664×832 . The

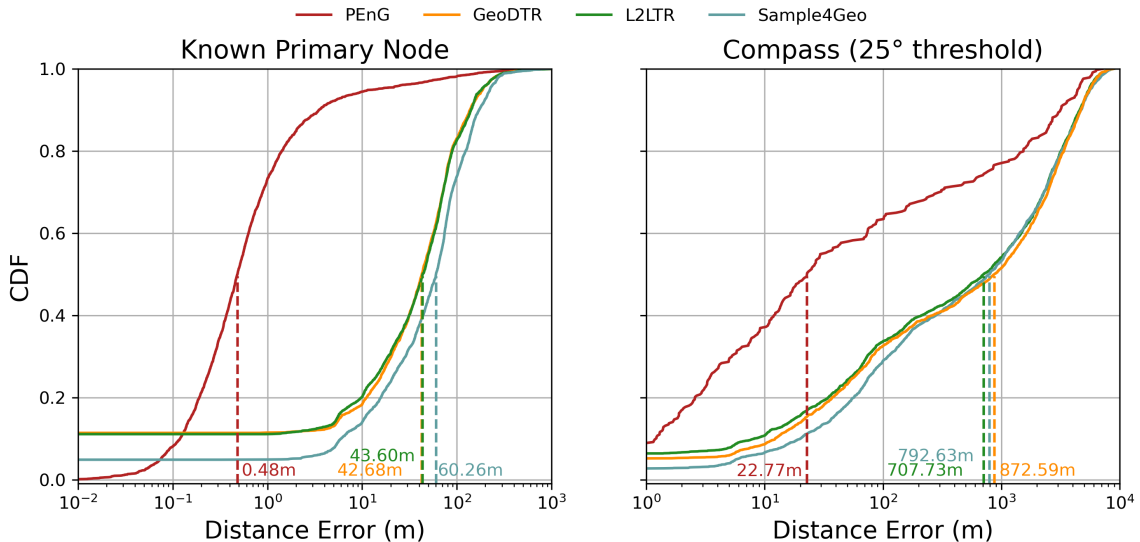


Fig. 6: Cumulative Distribution Functions show the significant decrease in distance error achieved with PEnG. Previous works are non-zero at $x = 0$ as there is 0m error when they correctly retrieve the corresponding correct satellite image.

median distance between the primary nodes is 116m, and the median distance between adjacent secondary nodes is 9.83m. As both training and evaluation datasets contain camera yaw values at image capture, we are able to produce limited-FOV front-facing crops, emulating a monocular camera - our expected input for real-world CVGL application for autonomous vehicles.

B. Implementation Details

Image features are extracted with a ConvNext-T [36] pre-trained on ImageNet-1K [37], producing 768-dimension embeddings. When evaluating against SpaGBOL [33] we instead use their trained feature extractor - a combination of a ConvNext-T CNN with a GraphSage GNN, generating low-dimensional vector representations. We perform this second evaluation with randomly sampled depth-first walks from the graph. We filter candidate edges by emulating a compass alongside the query, discarding incompatible graph edges. This is possible due to the graph representation - with known orientations between the primary node and its connected edges. All existing CVGL baselines are also augmented with this compass filtering technique to ensure a balanced assessment.

We use a median pose error threshold of 3° , halting execution if a match is found with a weighted euclidean distance below this. In the rare case that all edge pose estimates have an error larger than this threshold, the estimate with lowest error is selected. The feature extractor is trained with FOVs $\in \{70^\circ, 90^\circ, 120^\circ\}$ for 50 epochs using an AdamW optimiser with an initial learning rate of $1e-4$ and a ReduceLROnPlateau scheduler. The preset poses stored for reference points are calculated offline with a learning rate of 0.1 and 400 iterations, which are refined when online with a learning rate of 0.1 and 100 iterations.

Config	Med (m)	Top-1m	Top-5m	Top-25m
CVGL	961	6.06	6.94	9.27
1 Pose	32.12	7.02	25.45	45.12
2 Pose	28.94	7.31	26.41	47.91
Pose Priors	22.77	9.12	29.18	51.37

TABLE I: Successive ablation of PEnG stages to demonstrate the contribution of each, with 90° horizontal FOV.

C. Ablation Study

To verify the contribution of each constituent in the proposed system, we display an ablation study in Table I. CVGL shows the performance of the simple ConvNext-T feature extractor, evaluated in the same method as previous works - filtering by primary nodes initially to reduce the reference set. *1 Pose* performs pose estimation against an entire edge's reference images, determining a relative 2-DoF pose between primary nodes. *2 Pose* follows *1 Pose* with a refined pose estimation relative to the 2 adjacent reference secondary nodes, determined in the first pose estimation step - this enables a high precision final estimate. *Pose Priors* is the addition of estimating the pose of all secondary nodes prior to querying, increasing the accuracy of reference poses and offloading a portion of computation to an offline stage.

The ablation shows the vast decrease in median distance error achieved by combining these two localisation techniques, the median error decreases by an order of magnitude. Having a pose refinement stage after the initial position estimation further decreases median error by $\approx 3m$. Finally, estimating reference poses prior to operation increased accuracy relatively by $\approx 10\%$.

D. Evaluation

We evaluate with distance-based Top-K recall accuracy, displaying euclidean distance errors in Cumulative Distribu-

Model	Med (m)	Top-1m	Top-5m	Top-25m
FOV	70°			
L2LTR [38]	826	6.48	7.55	10.03
GeoDTR+ [31]	903	5.19	6.03	8.47
Sample4Geo [32]	897	6.79	7.78	10.41
PEnG	26.82	7.25	27.43	49.01
SpaGBOL [33]	634	6.37	7.70	10.56
PEnG*	<i>29.31</i>	<i>6.86</i>	<i>26.16</i>	<i>47.75</i>
FOV	90°			
L2LTR [38]	750	6.64	8.01	10.64
GeoDTR+ [31]	854	6.06	7.25	9.80
Sample4Geo [32]	734	8.35	9.31	12.43
PEnG	22.77	9.12	29.18	51.37
SpaGBOL [33]	529	6.33	7.25	9.69
PEnG*	<i>34.91</i>	<i>7.17</i>	<i>25.10</i>	<i>47.29</i>
FOV	120°			
L2LTR [38]	732	7.82	9.19	12.05
GeoDTR+ [31]	893	6.75	7.63	10.60
Sample4Geo [32]	703	9.50	10.68	14.42
PEnG	37.72	4.04	21.21	44.93
SpaGBOL [33]	501	6.90	7.86	10.14
PEnG*	<i>45.46</i>	<i>3.36</i>	<i>22.04</i>	<i>44.24</i>

TABLE II: Localisation precision comparison to previous works with a stage 1 scoring 0.9 threshold. Best image pair method displayed in **bold**, best graph-based method shown in *italic*.

tion Function (CDF) plots - displayed in Figures 6. Table II shows discretised metrics for these functions, defining estimates as successful if they are within K-metres of the ground truth. We evaluate how PEnG performs with images of varying FOV, with higher-FOV cameras tending to be more expensive but able to capture more information. All comparisons follow the 2-stage process: first predicting the closest primary node, then estimating the closest position within the reduced subset of connected secondary nodes. To demonstrate the generality of the PEnG approach we present results with both a traditional retrieval first stage, PEnG, and a graph-based first stage, PEnG*.

To increase fairness in comparison against traditional single-stage CVGL works, we augment these baselines with a secondary refinement stage where the same technique is run again, but only required to match against the ground-truth satellite images of the corresponding secondary nodes. In a real-world use case this is infeasible, as the reference set cannot contain precisely geographically aligned ground truth satellite images. However, it serves to provide a stronger baseline for comparison.

The evaluation shows that our proposal achieves significant improvements over current SOTA. With 90° images, we achieve a 96.90%% reduction in median error, and an approximate 213%% increase in Top-5m accuracy. We note that using 90° FOV images achieves a relative decrease in the median error of $\approx 4\text{m}$ compared to 70°. This is due to the increase in information available to each stage. However, further increasing the FOV to 120° yields a decrease in localisation precision. This may be caused by the input image dimensionality limitation of our model - due to the

backbone pre-training, the maximum image resolution for the system is 512×384 , placing an upper bound on how much information can pass through the system. Another hindrance is experienced from extracting perspective images from a 360° panorama. When increasing the horizontal FOV beyond 90°, these crops begin to display visibly distortion.

Within the discretised Top-Km metrics, PEnG performs slightly worse than previous works where $K < 5$ due to the inherent zero error bias in existing CVGL works. As K reaches 25m, performance is significantly higher across Fields-of-View (FOVs). As precisely centred ground-truth corresponding satellite images are known for each query streetview image in CVGL, they tend to perform unrealistically well with these Top-K metrics. This peculiarity of previous evaluation protocols is visible in Figure 6 where at $x = 0$, previous works start from a non-zero values.

V. CONCLUSION & FUTURE WORK

We successfully propose and demonstrate the utility of combining graph-representations, CVGL, and relative pose estimation techniques. This ensemble is proven to be a viable strategy for progressing CVGL within a large city-scale environment towards practicality, reducing median distance errors from hundreds of metres down to often centimetre level accuracy. PEnG achieves SOTA localisation precision when evaluated within the Manhattan region of 36.1km^2 , reducing the median error from Sample4Geo’s previous best of 734m down to 22.77m when operating with 90° FOV. In our ablation studies, we thoroughly demonstrate the significance of each portion of the 2-stage architecture, validating that the combination results in the maximum precision possible for PEnG. We release code for converting the StreetLearn dataset into the graph representation outlined above, along with PEnG technique’s code and corresponding pretrained weights, enabling future works to build upon the technique and further evaluate this ensemble.

A. Future Work

Several aspects of this work will be the target for optimisation in order to further progress the field towards real-world application. Due to the vast disparity in viewpoint within CVGL, performance from the first stage limits the potential precision achieved in the second stage. A more probabilistic fusion technique could mitigate this. Furthermore, the second stage of PEnG, RPE, can be computationally costly compared to the first stage. There is a trade-off between accuracy and complexity, based on the number of iterations performed with RANSAC+PnP. Future work could explore sequential extensions of the technique, introducing temporal priors into the position estimation, to further filter the reference set and reduce the number of iterations required.

VI. ACKNOWLEDGEMENTS

This work was partially funded by the EPSRC under grant agreement EP/S035761/1 and FlexBot - InnovateUK project 10067785.

REFERENCES

- [1] Piotr Mirowski, Andras Banki-Horvath, Keith Anderson, Denis Teplyashin, Karl Moritz Hermann, Mateusz Malinowski, Matthew Koichi Grimes, Karen Simonyan, Koray Kavukcuoglu, Andrew Zisserman, and Raia Hadsell. The streetlearn environment and dataset, 2019.
- [2] Eric Royer, Maxime Lhuillier, Michel Dhome, and Jean-Marc Lavest. Monocular Vision for Mobile Robot Localization and Autonomous Navigation. *International Journal of Computer Vision*, 74(3):237–260, 2007.
- [3] Arnold Irschara, Christopher Zach, Jan-Michael Frahm, and Horst Bischof. From structure-from-motion point clouds to fast location recognition. In *2009 IEEE Conference on Computer Vision and Pattern Recognition*, pages 2599–2606, 2009.
- [4] Torsten Sattler, Bastian Leibe, and Leif Kobbelt. Efficient & effective prioritized matching for large-scale image-based localization. *IEEE Transactions on Pattern Analysis and Machine Intelligence*, 39(9):1744–1756, 2017.
- [5] Jamie Shotton, Ben Glocker, Christopher Zach, Shahram Izadi, Antonio Criminisi, and Andrew William Fitzgibbon. Scene coordinate regression forests for camera relocalization in rgb-d images. *2013 IEEE Conference on Computer Vision and Pattern Recognition*, pages 2930–2937, 2013.
- [6] Alex Kendall, Matthew Grimes, and Roberto Cipolla. Posenet: A convolutional network for real-time 6-dof camera relocalization. In *Proceedings of the IEEE international conference on computer vision*, pages 2938–2946, 2015.
- [7] Alex Kendall and Roberto Cipolla. Geometric loss functions for camera pose regression with deep learning, 2017.
- [8] Eric Brachmann, Alexander Krull, Sebastian Nowozin, Jamie Shotton, Frank Michel, Stefan Gumhold, and Carsten Rother. Dsac - differentiable ransac for camera localization, 2018.
- [9] Ronald Clark, Sen Wang, Andrew Markham, Niki Trigoni, and Hongkai Wen. Vidloc: A deep spatio-temporal model for 6-dof video-clip relocalization, 2017.
- [10] Paul-Edouard Sarlin, Cesar Cadena, Roland Siegwart, and Marcin Dymczyk. From coarse to fine: Robust hierarchical localization at large scale. In *CVPR*, 2019.
- [11] Eduardo Arnold, Jamie Wynn, Sara Vicente, Guillermo Garcia-Hernando, Áron Monszpart, Victor Adrian Prisacariu, Daniyar Turmukhambetov, and Eric Brachmann. Map-free visual relocalization: Metric pose relative to a single image. In *ECCV*, 2022.
- [12] Chris Rockwell, Nilesh Kulkarni, Linyi Jin, Jeong Joon Park, Justin Johnson, and David F. Fouhey. Far: Flexible, accurate and robust 6dof relative camera pose estimation. In *CVPR*, 2024.
- [13] Shuzhe Wang, Vincent Leroy, Yohann Cabon, Boris Chidlovskii, and Jerome Revaud. Dust3r: Geometric 3d vision made easy. In *CVPR*, 2024.
- [14] Vincent Leroy, Yohann Cabon, and Jérôme Revaud. Grounding image matching in 3d with mast3r, 2024.
- [15] Arthur Moreau, Nathan Piasco, Moussab Bennehar, Dzmitry Tsishkou, Bogdan Stanciulescu, and Arnaud de La Fortelle. Crossfire: Camera relocalization on self-supervised features from an implicit representation. In *Proceedings of the IEEE/CVF International Conference on Computer Vision*, pages 252–262, 2023.
- [16] Sijie Zhu, Mubarak Shah, and Chen Chen. Transgeo: Transformer is all you need for cross-view image geo-localization. *2022 IEEE/CVF Conference on Computer Vision and Pattern Recognition (CVPR)*, pages 1152–1161, 2022.
- [17] Yingying Zhu, Hongji Yang, Yuxin Lu, and Qiang Huang. Simple, effective and general: A new backbone for cross-view image geo-localization, 2023.
- [18] Tavis Shore, Simon Hadfield, and Oscar Mendez. Bev-cv: Birds-eye-view transform for cross-view geo-localisation, 2023.
- [19] Scott Workman and Nathan Jacobs. On the location dependence of convolutional neural network features. In *2015 IEEE Conference on Computer Vision and Pattern Recognition Workshops (CVPRW)*, pages 70–78, 2015.
- [20] Tsung-Yi Lin, Yin Cui, Serge Belongie, and James Hays. Learning deep representations for ground-to-aerial geolocalization. In *2015 IEEE Conference on Computer Vision and Pattern Recognition (CVPR)*, pages 5007–5015, 2015.
- [21] Nam N. Vo and James Hays. Localizing and orienting street views using overhead imagery. In *European Conference on Computer Vision*, 2016.
- [22] Sixing Hu, Mengdan Feng, Rang M. H. Nguyen, and Gim Hee Lee. Cvm-net: Cross-view matching network for image-based ground-to-aerial geo-localization. In *2018 IEEE/CVF Conference on Computer Vision and Pattern Recognition*, pages 7258–7267, 2018.
- [23] Relja Arandjelović, Petr Gronát, Akihiko Torii, Tomás Pajdla, and Josef Sivic. Netvlad: Cnn architecture for weakly supervised place recognition. *IEEE Transactions on Pattern Analysis and Machine Intelligence*, 40:1437–1451, 2015.
- [24] Liu Liu and Hongdong Li. Lending orientation to neural networks for cross-view geo-localization. In *2019 IEEE/CVF Conference on Computer Vision and Pattern Recognition (CVPR)*, pages 5617–5626, 2019.
- [25] Yujiao Shi, Liu Liu, Xin Yu, and Hongdong Li. Spatial-aware feature aggregation for image based cross-view geo-localization. In *Neural Information Processing Systems*, 2019.
- [26] Yujiao Shi, Xin Yu, Liu Liu, Tong Zhang, and Hongdong Li. Optimal feature transport for cross-view image geo-localization. *ArXiv*, 2019.
- [27] Yujiao Shi, Xin Yu, Dylan Campbell, and Hongdong Li. Where am i looking at? joint location and orientation estimation by cross-view matching. *2020 IEEE/CVF Conference on Computer Vision and Pattern Recognition (CVPR)*, pages 4063–4071, 2020.
- [28] Aysim Toker, Qunjie Zhou, Maxim Maximov, and Laura Leal-Taix'e. Coming down to earth: Satellite-to-street view synthesis for geo-localization. *2021 IEEE/CVF Conference on Computer Vision and Pattern Recognition (CVPR)*, pages 6484–6493, 2021.
- [29] Hongji Yang, Xiufan Lu, and Ying J. Zhu. Cross-view geo-localization with layer-to-layer transformer. In *Neural Information Processing Systems*, 2021.
- [30] Xiaohan Zhang, Xingyu Li, Waqas Sultani, Yi Zhou, and Safwan Wshah. Cross-view geo-localization via learning disentangled geometric layout correspondence, 2023.
- [31] Xiaohan Zhang, Xingyu Li, Waqas Sultani, Chen Chen, and Safwan Wshah. Geodtr+: Toward generic cross-view geolocalization via geometric disentanglement, 2023.
- [32] Fabian Deuser, Konrad Habel, and Norbert Oswald. Sample4geo: Hard negative sampling for cross-view geo-localisation, 2023.
- [33] Tavis Shore, Oscar Mendez, and Simon Hadfield. Spagbol: Spatial-graph-based orientated localisation, 2024.
- [34] Martin A. Fischler and Robert C. Bolles. Random sample consensus: a paradigm for model fitting with applications to image analysis and automated cartography. *Commun. ACM*, 24(6):381–395, June 1981.
- [35] Scott Workman, Richard Souvenir, and Nathan Jacobs. Wide-area image geolocalization with aerial reference imagery. In *IEEE International Conference on Computer Vision (ICCV)*, pages 1–9, 2015. Acceptance rate: 30.3%.
- [36] Zhuang Liu, Hanzi Mao, Chao-Yuan Wu, Christoph Feichtenhofer, Trevor Darrell, and Saining Xie. A convnet for the 2020s. *Proceedings of the IEEE/CVF Conference on Computer Vision and Pattern Recognition (CVPR)*, 2022.
- [37] Jia Deng, Wei Dong, Richard Socher, Li-Jia Li, Kai Li, and Li Fei-Fei. Imagenet: A large-scale hierarchical image database. In *2009 IEEE Conference on Computer Vision and Pattern Recognition*, pages 248–255, 2009.
- [38] Hongji Yang, Xiufan Lu, and Yingying Zhu. Cross-view geo-localization with layer-to-layer transformer. In M. Ranzato, A. Beygelzimer, Y. Dauphin, P.S. Liang, and J. Wortman Vaughan, editors, *Advances in Neural Information Processing Systems*, volume 34, pages 29009–29020. Curran Associates, Inc., 2021.